




Article

Determination of Air Urban Heat Island Parameters with High-Precision GPS Data

Jorge Mendez-Astudillo ¹, Lawrence Lau ^{2,*}, Yu-Ting Tang ³ and Terry Moore ⁴

¹ Instituto de Geografía, Universidad Nacional Autónoma de México, Mexico City 04510, Mexico; jmendez@igg.unam.mx

² Department of Land Surveying and Geo-Informatics, The Hong Kong Polytechnic University, Hong Kong, China

³ School of Geographical Sciences, University of Nottingham Ningbo China, Ningbo 315104, China; yu-ting.tang@nottingham.edu.cn

⁴ The Nottingham Geospatial Institute, The University of Nottingham, Nottingham NG7 2RD, UK; terry.moore@nottingham.ac.uk

* Correspondence: lsgj-lawrence.lau@polyu.edu.hk

Abstract: The urban heat island (UHI) effect can contribute to extreme heat exposure. This can be detrimental to human health. In this paper, we propose a method to estimate air temperature to evaluate the spatial distribution and to monitor the intensity of the air urban heat island (AUHI) from existing GPS infrastructure. The proposed algorithm is based on the relationship between the refractivity of the troposphere and environmental variables, as well as the relationships between the zenith tropospheric delay (ZTD), a by-product of the precise point positioning technique, and the refractivity of the troposphere. The advantage of GPS data is its high temporal resolution and the availability of embedded GPS receivers. In this paper, GPS-derived ZTD data from stations in the Hong Kong Special Administrative Region (HKSAR) of China and Tokyo in Japan are processed to estimate the hourly AUHI intensity. The results derived from this technique are validated using meteorological data in the same cities. Mean absolute error values of 0.79 °C in Hong Kong and 0.22 °C in Tokyo are found from data from the summer. Moreover, an overall accuracy of 0.51 °C is found.

Keywords: urban heat island; GPS meteorology remote sensing; precise point positioning; tropospheric delay; zenith tropospheric delay; UHI diurnal cycle; Hong Kong; Tokyo



Citation: Mendez-Astudillo, J.; Lau, L.; Tang, Y.-T.; Moore, T. Determination of Air Urban Heat Island Parameters with High-Precision GPS Data. *Atmosphere* **2022**, *13*, 417. <https://doi.org/10.3390/atmos13030417>

Academic Editors: Matthew Eastin and Ferdinando Salata

Received: 26 January 2022

Accepted: 27 February 2022

Published: 3 March 2022

Publisher's Note: MDPI stays neutral with regard to jurisdictional claims in published maps and institutional affiliations.



Copyright: © 2022 by the authors. Licensee MDPI, Basel, Switzerland. This article is an open access article distributed under the terms and conditions of the Creative Commons Attribution (CC BY) license (<https://creativecommons.org/licenses/by/4.0/>).

1. Introduction

The urban heat island (UHI) is a direct consequence of urbanization and industrialization, and is detected when an urban area is warmer than its rural surroundings [1]. According to the United Nations, urbanization has increased around the world, and another 2.5 billion people are expected to move to urban areas by 2050 [2]. With this growth in urbanization, an intensification of the UHI effect is expected in several cities around the world [3], along with greater exposure to extreme heat, especially for vulnerable populations [4].

Exposure to extreme heat can have adverse effects on human health; for instance, the “heat stroke” is a consequence of extreme heat exposure. Exposure to extreme heat and high humidity can produce adverse health consequences such as cardiopulmonary problems in high-risk groups and can cause sleep disruption, which is associated with impaired cognitive performance [5]. In order to mitigate UHI and the effects it has on human health and energy consumption, it is necessary to possess tools to monitor the UHI effect.

The surface UHI (SUHI) is monitored via land surface temperature values obtained from satellites such as LANDSAT 8 [6]. The UHI based on air temperatures (AUHI) is monitored using a network of ground-based temperature sensors from weather stations in

urban and rural areas [7]. The main disadvantage of temperature sensors is the high costs associated with deploying and maintaining the large network of weather sensors needed to cover a metropolitan area. An alternative to ground-based temperature sensors, is the use of global navigation satellite system (GNSS) signals, specifically from the Global Positioning System (GPS), to remotely sense the atmosphere [8] based on the delay caused by the troposphere (proportional to the troposphere's physical properties) as the GPS signals propagate through the troposphere from the satellite to the receiver near the ground.

For example, GPS data have been used to measure precipitable water with an RMS error of 4.6 mm compared with MODIS [9], or with no statistical difference compared with MODIS in a tropical region [10]. The advantage of using GPS signals for remote sensing is that GPS data have high temporal resolution and can be obtained in real-time [11]. Furthermore, GPS data are available under any weather conditions. Moreover, GPS receivers are widely available in handheld devices such as smartphones, which can be used to collect GPS data and perform the precise point positioning (PPP) [12]. Therefore, dense sensor networks can be built with existing GPS infrastructure at no added cost. The use of embedded GPS receivers can contribute to producing high-quality digital data in the big data era.

In this paper, we propose an adaptation to the method to estimate temperature using the PPP-derived ZTD from ground-based GNSS observations [13] to make it useful for hourly GPS data. Estimated hourly temperatures are then used to assess the diurnal cycle of the air urban heat island (AUHI) in Hong Kong (HK) and Tokyo. The approach is tested with GPS data from 2016 to 2019 from 10 GNSS stations located in Hong Kong and 3 GPS stations in Tokyo. Furthermore, temperature data from weather stations in both cities are used for validation. There were 6055 billion smartphone users in the world as of 2020 [14], and each smartphone has an embedded GPS receiver. Therefore, this GPS-data-based method has great practical potential to be implemented in smartphones and make spatial AUHI data available for big data applications.

Previous studies on the UHI effect in Hong Kong (HK) have used mobile weather stations in a few points across HK [15–17]. Additionally, satellite data have been used to estimate AUHI in HK [18,19]. Other studies have used data from the meteorological networks provided by the Hong Kong Observatory to study the AUHI [20,21]. In both cases, the weather station in the Hong Kong Observatory's headquarters in Tsim Sha Tsui was considered as an urban station. However, rural stations have been defined differently; the station in Tsak Yue Wu [20] and the one in Ta Kwu Ling [21] have both been defined as rural. Siu and Hart [20] found that a maximum intensity of 2.5 °C occurs at around 20:00 local time. Using meteorological data for UHI evaluation in HK, Chen and Jeong [21] found that the UHI during July is approximately 0.7 °C, while during December the UHI intensity is around 1.5 °C. The approach presented here provides air temperature data at new locations, which enables the study of the spatial distribution of the AUHI in HK.

In Tokyo, the AUHI intensity has been previously measured using meteorological data from the Automated Meteorological Data Acquisition System (AMeDAS) managed by Japan Meteorological Agency JMA [22]. Hirano and Fujita [23] used air temperature data from JMA to study the impacts of energy consumption on the UHI in Tokyo. Other studies of AUHI using data from JMA are the study of UHI changes with the changes of the city and the effects of urbanization on rainfall [24] and Varquez and Kanda's [25] global study of the UHI. Furthermore, the AUHI in Tokyo has been measured using machine learning techniques and JMA data from 2015–2019 [26].

2. Study Areas and Datasets

The two reasons for choosing Hong Kong and Tokyo for this study are that both cities are major agglomerations in Asia and the difference in geography is advantageous to show the potential use of this AUHI monitoring approach. Hong Kong is a very mountainous region; therefore, the urban agglomeration is found in flat land and the population density is very high. Therefore, urban and rural stations for AUHI monitoring are defined using

the local climate zone definition [27]. On the other hand, Tokyo lays mostly on flat land; therefore, the stations in rural areas outside of the main urban agglomeration were used to monitor the AUHI. Additionally, both cities have a well-developed PS network in their territory covering different parts of the cities. Moreover, both cities have a robust meteorological sensor network providing weather data covering the whole city and different LCZs, which is advantageous for validation of the proposed algorithm.

2.1. Study Area: Hong Kong

Hong Kong (HK) ($22^{\circ}17'7.87''$ N, $114^{\circ}9'27.68''$ E) is a Special Administrative Region (SAR) of China located to the east of the Pearl River estuary on the south coast of China. The region is bordered by Guangdong province in China and the South China Sea to the east, south, and west. HK is located at the northern fringe of the tropical climate zone. Because of the location, monsoonal seasonal changes are well delineated with hot and humid summers and dry and cool winters. According to the latest data of the census and statistics department, HK has around 7,500,000 inhabitants and the territory has a total land area of 1050 km². Thus, Hong Kong is considered a 100% urban area [2]; however, patches of rural-like areas are found in the mountainous regions and islands surrounding the urban core. Therefore, there are different local climate zones that enable the study of the UHI using LCZ.

2.2. Study Area: Tokyo, Japan

Tokyo ($35^{\circ}41'123''$ N $139^{\circ}41'32''$ E) is the capital city of Japan and its largest agglomeration. Located at the head of Tokyo Bay on the pacific coast of central Honshu Island, it is characterized by a humid subtropical climate zone with hot and humid summers and cool winters. The warmest and coolest months are August with an average temperature of 28 °C and February with an average temperature of 7 °C, respectively [28]. According to the Statistics Bureau of Japan, 36,130,685 inhabitants live in the Tokyo metropolitan area, including the prefectures of Kanagawa, Saitama, and Chiba. The Tokyo metropolitan area covers 13,500 km² and is mostly on flat land [29].

2.3. GPS and Meteorological Datasets Used in Algorithm

2.3.1. GPS Data Used to Estimate UHII

In HK, raw GPS observation data are provided by the Hong Kong Geodetic Survey Services [30], a part of the Lands Department of the Survey and Mapping Office of Hong Kong Special Administrative Region. HKGSS manages 18 stations in HK, and their data can be downloaded from the HKGSS ftp server [30] at different time intervals of 1 s, 5 s and 30 s. Data from two stations in HK (namely HKWS and HKSL) can also be accessed through the International GNSS Service (IGS). In Tokyo, the IGS manages 3 GNSS stations in the Tokyo metropolitan area plus 3 other GNSS stations in surrounding rural areas. GNSS data provided by the IGS are available in the IGS server [31].

In this study, we processed GPS data from 6 stations in HK. Stations were selected based on the meteorological data availability and the local climate zone. For the Tokyo area, we used the data from 3 GPS stations, 2 in the Tokyo area and one in Tsukuba, which is a rural area near Tokyo. The descriptions of the three stations in the Tokyo metropolitan area and the 6 stations in Hong Kong chosen for this study are shown in Table 1, while the sources of data are marked as “GEO” if collected from HKGSS and “IGS” if collected from the IGS.

2.3.2. Meteorological Data Used for Validation

In Hong Kong, both the HKGSS and the IGS provide meteorological data at the same locations as GNSS data are provided. The following meteorological variables are reported every minute: pressure, temperature, and relative humidity. In Japan, the JMA operates seven stations in the Tokyo Metropolitan area that report hourly temperature, precipitation amount, snow depth, wind direction and speed, sunshine duration, surface pressure, and

relative humidity values. However, only 3 stations were chosen for the validation of the algorithm because they cover urban- and rural-like areas. Table 1 describes the weather stations from the JMA used for validation purposes.

Table 1. Selected GPS and meteorological stations used in this study to monitor the AUHI intensity levels in Hong Kong and Tokyo.

	Code	GNSS Data	Meteorological Data	Source	Site	Coordinates (deg)
Hong Kong	HKKT	X	X	GEO	Kam Tim	22.44, 114.06
	HKPC	X	X	GEO	Peng Chau	22.28, 114.03
	HKSC	X	X	GEO	Stonecutters Island	22.32, 114.14
	HKSL	X	X	IGS	Siu Lang Shui	22.37, 113.93
	HKWS	X	X	IGS	Wong Shek	22.43, 114.33
	T430	X	X	GEO	Fan Ling	22.49, 114.14
Tokyo	KGNI	X		IGS	Koganei	35.71, 139.48
	MTKA	X		IGS	Mitaka	35.67, 139.56
	TSKB	X		IGS	Tsukuba	36.1, 140.08
	TOK		X	JMA	Chiyoda	35.69, 139.75
	HND		X	JMA	Haneda Airport	35.53, 139.78
	NER		X	JMA	Shakuji Park	35.75, 139.59

The locations of GPS stations in Hong Kong and GPS stations and weather stations in the Tokyo metropolitan area are shown in the map shown in Figure 1. Figure 1a shows the locations in Hong Kong of GPS and meteorological stations, and temperature and GPS data are reported from the same sites. Figure 1b shows the locations of GPS stations (black points) and meteorological stations (green points) in Tokyo.

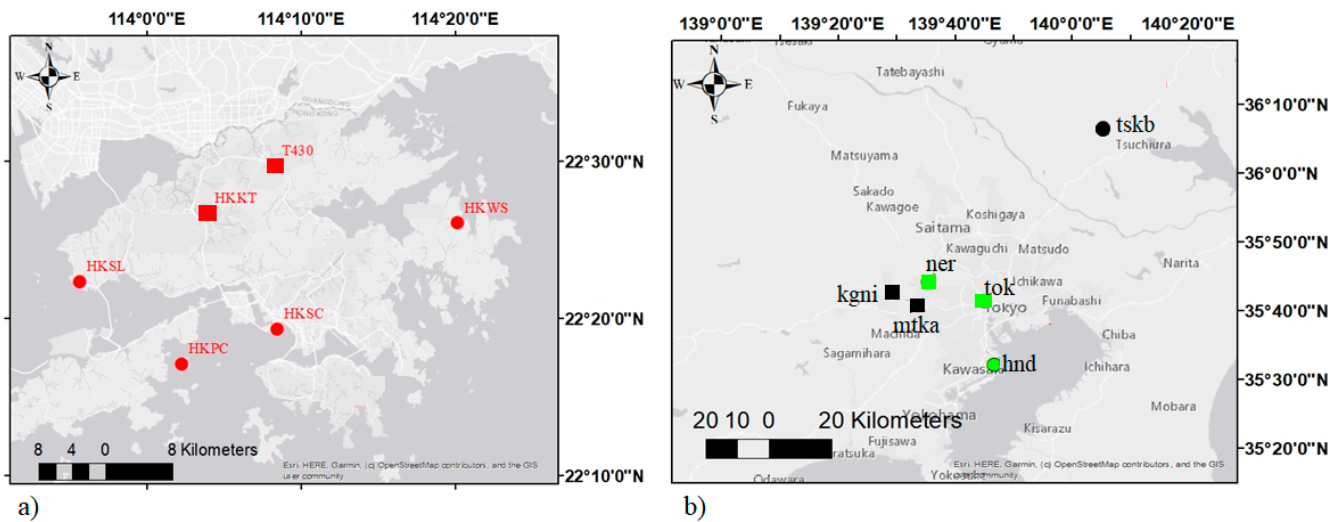


Figure 1. (a) Locations of GPS and meteorological stations in Hong Kong. (b) The locations of GPS stations and meteorological stations in Tokyo used for this study. Black points are GPS stations and green points are meteorological stations. Squares are urban stations and circles are rural or rural-like stations.

2.3.3. Data Used for Classification of Surroundings of Stations

Satellite images provided by Google Earth were used to classify the surroundings of the stations into different LCZs [27]. The satellite images from Hong Kong were taken in September 2019. Note that the surroundings of the stations in HK did not change significantly during the period 2016–2019.

2.3.4. Radiosonde Data Used in the Algorithm

Radiosonde data were used to calculate the height of the tropopause and “universal values” required by the algorithm. Here, 10 years of data from 2009–2019 were collected from two radiosondes from the Integrated Global Radiosonde Archive were used in this study [32]: radiosonde HKM00045004 located in Kowloon, Hong Kong, latitude = 22.33°, longitude = 114.16°, height = 24 m; radiosonde JAM00047646 located near Tsukuba, Japan, latitude = 36.05°, longitude = 140.12°, height = 25.2 m.

3. Local Climate Zone Classification



The local climate zone (LCZ) classification is used to classify stations for urban climate studies depending on their surroundings. The LCZ approach classifies the landscape of a given area into 19 local climate zones according to surface cover and surface structure. Additionally, four landscape series are used, which can be either city, agricultural, natural, or mixed [27,33].

Stations surrounded by tall buildings and urban infrastructure are considered urban stations. Furthermore, we considered anthropogenic heat sources such as highways with lots of traffic or certain parts of industrial structures in the same urban category. The classification of an LCZ is achieved by defining a 250 m radius around the station and visually detecting the type of land cover surrounding the station.

3.1. Urban Stations in Hong Kong and Tokyo

In HK, station HKKT is located in Kam Tim, surrounded by open low-rise buildings and two main highways. Station T430 is located in Fan Ling near two highways and an area of compact high-rise buildings. The surroundings of the urban stations and the classification in the LCZ system are shown in Table 2. In Tokyo, the classification of stations type is achieved by defining rural stations far away from the urban core of the city with different land cover and land uses. Therefore, the GNSS stations MTKA and KGNI are classified as urban stations. Similarly, TOK and NER meteorological stations are considered urban stations.

Table 2. Urban stations in Hong Kong.

HKKT (GPS + met) Kam Tim	T430 (GPS + met) Fan Ling
	
LCZ 6A	LCZ 4
Surrounded by vegetation, some open low-rise structures and a highway.	Surrounded by compact high-rise structures and open low high-rise structures.

3.2. Rural Stations in Hong Kong and Tokyo

The other 4 chosen stations in Hong Kong described in Table 1 are defined as being in rural areas because they are surrounded mostly by vegetation, big bodies of water, or a few built structures. Furthermore, several anthropogenic heat sources are found within a radius of 500 m around the stations. The remaining four stations in HK were classified as rural. Furthermore, one GPS station (TSKB) and one meteorological station (Haneda) in Tokyo are classified, as rural stations as in Table 3. The satellite photos used to classify as urban or rural based on the station's surroundings are shown in Appendix A (Figures A1 and A2).

Table 3. GPS and meteorological stations in rural-like areas in Hong Kong and Tokyo.

	Code	Site	LCZ	Description
Hong Kong GNSS + met	HKLT	Lam Tei	A	Surrounded by vegetation.
	HKOH	Shek O	A	Surrounded by vegetation.
	HKPC	Peng Chau	G ₇	Surrounded by sea and open low-rise.
	HKSC	Stonecutters Island	A ₆	Surrounded by vegetation and open low-rise.
	HKSL	Siu Lang Shui	10 _C	Industrial area nearby and vegetation.
	HKSS	Tseng Tau Tsuen	B _G	Surrounded by vegetation and compact low-rise, seashore nearby.
	HKST	Fo Tan	B ₆	Surrounded by vegetation and open low-rise.
	HKWS	Wong Shek	A _G	Surrounded by vegetation water body nearby.
Tokyo GNSS	TSKB	Tsukuba	A ₉	Surrounded by vegetation and sparsely built structures. The station is 65 km away from Tokyo's urban core.
Tokyo met	HND	Haneda airport	E ₉	Surrounded by pavement, and sparsely built structures.

4. Algorithm to Estimate Temperature from GPS Data

As the GPS signal propagates through the atmosphere from the satellite to the receiver, a delay is induced by the different layers of the atmosphere. The layers that have the greatest effects on the propagating GPS signals are the ionosphere and the troposphere. However, positioning algorithms use a combination of dual-frequency GPS data to eliminate most of the ionospheric delay. Therefore, in this section the focus will be on the tropospheric delay. The algorithm developed to calculate the UHI intensity (UHII) from hourly GPS data is divided into three steps:

1. GPS observation data are processed using the PPP technique to obtain the ZTD and location coordinates of the station.
2. Calculation of temperature using ZTD in both urban and rural stations.
3. Computation of the intensity of the UHI effect.

4.1. Step 1: Estimation of ZTD

The troposphere causes a delay to the propagating GPS signal proportional to the environmental variables around the receiver, namely air pressure, water vapor partial pressure, and temperature. The tropospheric delay in the zenith direction (ZTD) is a by-product of the precise point positioning (PPP) technique, which is implemented with an extended Kalman filter to estimate location coordinates and other parameters such as ZTD using GNSS observation data, GPS navigation data, and precise ephemeris [34]. One of the advantages of the PPP technique is that it can achieve centimeter precision and only one receiver is needed to estimate locations and other parameters around the receiver [35].

There are several implementations of the PPP technique in stand-alone software and online services that have been compared, and it has been shown that the open-source

software RTKLIB achieves estimations with high precision [36]. Therefore, RTKLIB was chosen as the GPS data processing software. RTKLIB can implement different positioning techniques, among them the PPP technique, in either statistic or kinematic mode. RTKLIB requires GPS observation data, a precise ephemeris, a clock, and navigation data, which were obtained from the final IGS products to estimate locations and ZTD. In this study, 4 years (2016–2019) of ground-based GPS observation data described in Table 1 were processed with RTKLIB in kinematic mode and a ZTD estimation was obtained every 30 s.

4.2. Step 2: ZTD Based Temperature Derivation

The algorithm used to estimate temperature values from GPS data is divided into three parts, namely the calculation of universal parameters, the calculation of local parameters, and the calculation of temperatures [13]. The first step of the algorithm requires known values for the height of the troposphere (Z_{trop}), air pressure at the place of measurement (P), and water vapor partial pressure (e) at the site of measurement to compute the profile of the refractivity. These values are obtained from radiosonde data and are called the universal parameters. This algorithm was developed and tested with daily averages from stations in Los Angeles and an accuracy of 1.71 °C has been achieved [13]. We adapted the algorithm to handle hourly averages and increase its accuracy.

4.2.1. Height of the Troposphere (Z_{trop})

The height of the troposphere Z_{trop} is a very important parameter in this algorithm. It was calculated using radiosonde data in Hong Kong and Tokyo and the criteria for the first and second lapse rate tropopause (LRT1 and LRT2) defined by the World Meteorological Organization (WMO). The LRT1 is defined as the lowest level at which the lapse rate (change of temperature with height) decreases to 2 °C/km or less, provided also that the averaged lapse rate between this level and levels within the next 2 km vertically does not exceed 2 °C/km. If above the LRT1 the average lapse rate between any level and all higher levels within 1 km exceeds 3 °C/km, then a second tropopause (LRT2) is defined. LRT2 may be either within or above the 1 km layer. The Z_{trop} is defined as the height of LRT2.

4.2.2. Pressure (P)

Hourly pressure data were obtained from the meteorological stations described in Table 1.

4.2.3. Water Vapor Pressure

In a previous study [13], daily averages of GNSS and meteorological data were used to monitor the UHI intensity. In contrast, in this study, hourly GNSS and meteorological data were processed to detect the diurnal cycle of the temperature and increase the algorithm's temporal resolution. The use of hourly data meant we had to change the strategy to estimate the water vapor pressure needed in the algorithm.

Previously, the water vapor pressure e near the receiver had been estimated using Antoine's model and temperatures from the first height of a radiosonde sounding [13]. The use of radiosonde data (one sounding or in some cases two soundings per day) and the fact that Antoine's model depends on temperature are two mayor limitations of that approach. Therefore, in our approach, the water vapor pressure was derived from the definition of the relative humidity (RH) as the ratio of e water vapor pressure and e_s saturated water vapor pressure:

$$RH = \frac{e}{e_s} \quad (1)$$

and the definition of the water vapor pressure using the Classius–Clayperon equation and saturated water vapor [37]:

$$e_s = e_0 \exp \left[\frac{L}{R_v} \cdot \left(\frac{1}{T_0} - \frac{1}{T} \right) \right] \quad (2)$$

where R_v is the water vapor gas constant $461 \text{ JK}^{-1} \text{ kg}^{-1}$, T_0 is the absolute 0 temperature 273.15 K , $e_0 = 0.6113 \text{ kPa}$, and L is the latent heat parameter, which for water is $2.5 \times 10^6 \text{ JK}^{-1}$. Here, T is the air temperature in kelvins. RH and T data from meteorological stations in Hong Kong and Tokyo are used to compute e every hour.

4.2.4. ZTD and Environmental Variables

The tropospheric delay is related to the environmental conditions through the refractivity of the troposphere. The refractivity N of the troposphere is defined as [38]:

$$N = k_1 \cdot \frac{p - e}{T} + k_2 \cdot \frac{e}{T} + k_3 \cdot \frac{e}{T^2} \quad (3)$$

where the empirically calculated constants $k_1 = 77.6 \text{ K/hPa}$, $k_2 = 72 \text{ K/hPa}$, and $k_3 = 3.75 \times 10^5 \text{ K/hPa}$; P is the pressure of the air at the point of measurement, e is the water vapor partial pressure derived in Section 4.2.3, and the T is the temperature in Kelvin degrees. Hydrometeors and extreme weather events can affect the refractivity of the troposphere [39]. However, in this study, that effect was not considered because no hydrometeor or extreme weather event was reported during the period of this study (Jan–May 2016–2019).

The troposphere causes a delay to the signal in the zenith direction ZTD (in meters), which can be expressed as an integral of the total refractivity N along the propagation path s from receiver r to satellite w [38].

$$ZTD = 10^{-6} \int_r^w N ds \quad (4)$$

The refractivity of the troposphere changes at different altitudes because it is proportional to the temperature, which changes with altitude. The profile of the refractivity against altitude was empirically derived using ten years of radiosonde data in Hong Kong and Tokyo and Equation (3) for the different heights of reported radiosonde soundings [40]:

$$N = N_0 \exp^{-N_h z} \quad (5)$$

where N_0 is the refractivity at height equals to 0 m, N_h is the ratio of change of the refractivity with altitude, and Z is the height at which the measurement is taken. A local N_0 (N_{0_local}) is found using N_h , Z_{trop} (height of the tropopause), the altitude of the receiver (Z_{rec}), and the ZTD in Equation (5):

$$N_{0_local} = \frac{ZTD}{10^{-6} \int_{z_{rec}}^{z_{trop}} \exp^{-N_h z} dz} \quad (6)$$

Here, N_{0_local} is the value of the refractive index near the surface of the place of measurement. The PPP algorithm produced one value of ZTD every minute; therefore, every hour 60 ZTD values were averaged to obtain hourly ZTD .

The temperature of the site is calculated with GPS data by solving the quadratic equation:

$$N_{0_local} T^2 - T(k_1 P - (k_1 + k_2)e) - k_3 e = 0 \quad (7)$$

Daily, 1440 values (one per minute) of temperature were calculated. Hourly temperatures were taken every day from 2016 to 2019. All values at the same time and day in different years were averaged to find averaged hourly temperatures for each GPS station.

4.3. Step 3: GPS Based UHII Estimation

The AUHI intensity ($AUHII$) is calculated by subtracting the temperature at an urban station from the temperature at a rural station.

$$AUHII = T_{gnss}(URBAN) - T_{gnss}(RURAL) \quad (8)$$

where $T_{gps}(URBAN)$ and $T_{gps}(RURAL)$ are the temperatures estimated from GNSS data in urban and rural stations, respectively. In HK, there are two urban stations in warm LCZs, whereas in Tokyo there is only one urban station inside the main agglomeration. $T_{gps}(RURAL)$ is the temperature estimated in rural stations. In Hong Kong there are 4 rural stations, whereas in Tokyo there is only one rural station located in Tsukuba, 65 km away from the city center.

4.4. UHII Obtained with Meteorological Data

Meteorological data collected at the same locations as the GNSS stations in HK and in near locations in Tokyo, as described in Table 1, were used to measure $AUHII$ values.

$$AUHII = T_{met}(URBAN) - T_{met}(RURAL) \quad (9)$$

The temperatures measured at rural locations $T_{met}(RURAL)$ are subtracted from the temperatures measured in urban locations $T_{met}(URBAN)$. These UHII value are used to validate the algorithm.

5. Results and Discussion

The temperatures estimated with GPS data in Hong Kong and Tokyo were used to compute the spatial distribution of the $AUHII$ at day and night during the summer in both cities. These temperatures were then used to calculate the hourly profile of the $AUHII$ intensity levels in both cities. Finally, the results were validated by comparing them to the $AUHII$ obtained with meteorological data.

5.1. UHII in Hong Kong

Air temperatures in Hong Kong are higher during the summer and during the day; however, at night is when the UHII is higher. Therefore, the spatial distribution of the temperatures estimated with GPS data, as shown in Figure 2, was calculated with the average temperatures during the day (08:00–20:00 local time (UTC+8) LT) and night (20:00–08:00 LT) during the summer (June–August).

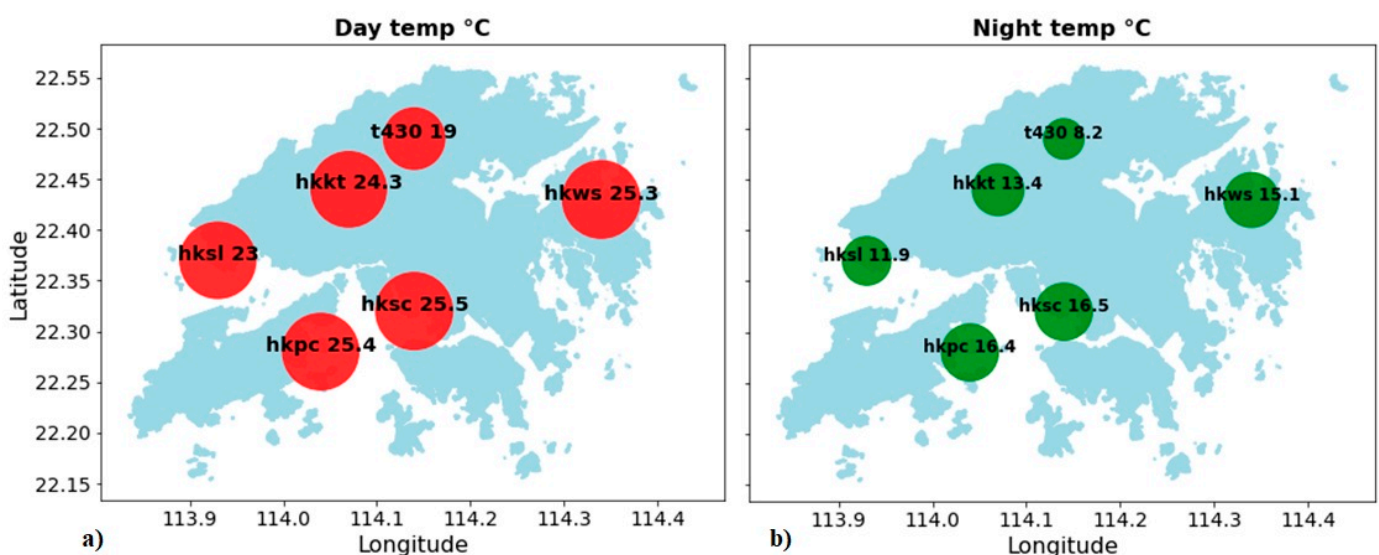


Figure 2. (a) Average temperatures derived from GPS data during the day in the summer. (b) Average temperatures derived from GPS data during the night in the summer.

The UHI intensity at night is higher than during the day, as shown in Figure 2b.

According to the profiles of the $AUHII$ intensity estimated with GPS data and the intensity measured with meteorological data shown in Figure 3, the intensity reaches its maximum value at 06:00 LT, after which the intensity decreases. Clearly, during the

morning hours (08:00–20:00 LT), the UHI Intensity profile is different to the profile during night-time (20:00–08:00 LT).

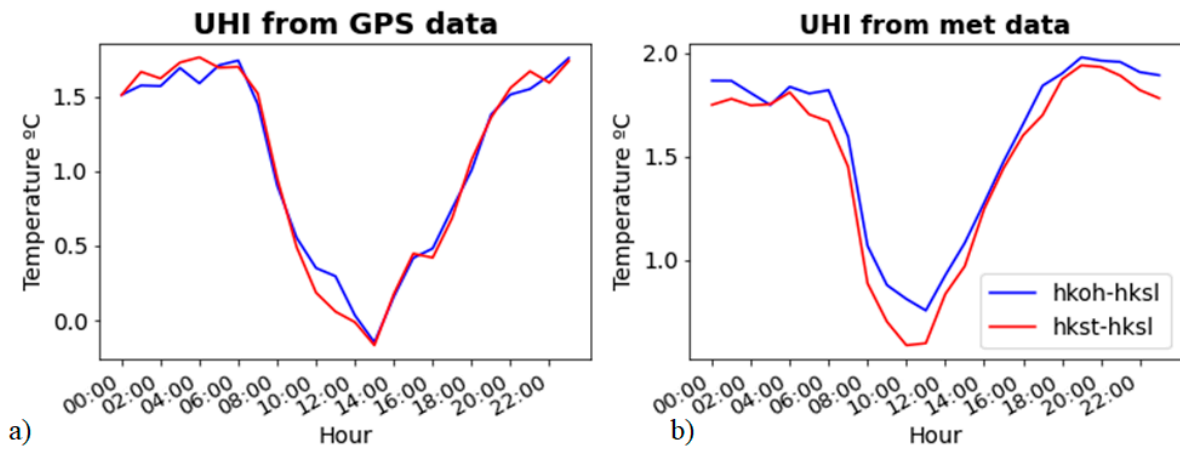


Figure 3. Diurnal cycle of AUHI intensity in Hong Kong with (a) GPS data and (b) meteorological data.

5.2. UHI in Tokyo

The spatial distributions of average temperatures estimated with this algorithm and GPS data during the day (08:00–20:00 LT) and night (20:00–08:00 LT) in the summer (June–September) in Tokyo are shown in Figure 4a,b, respectively. The air UHI was observed during the night rather than during the day.

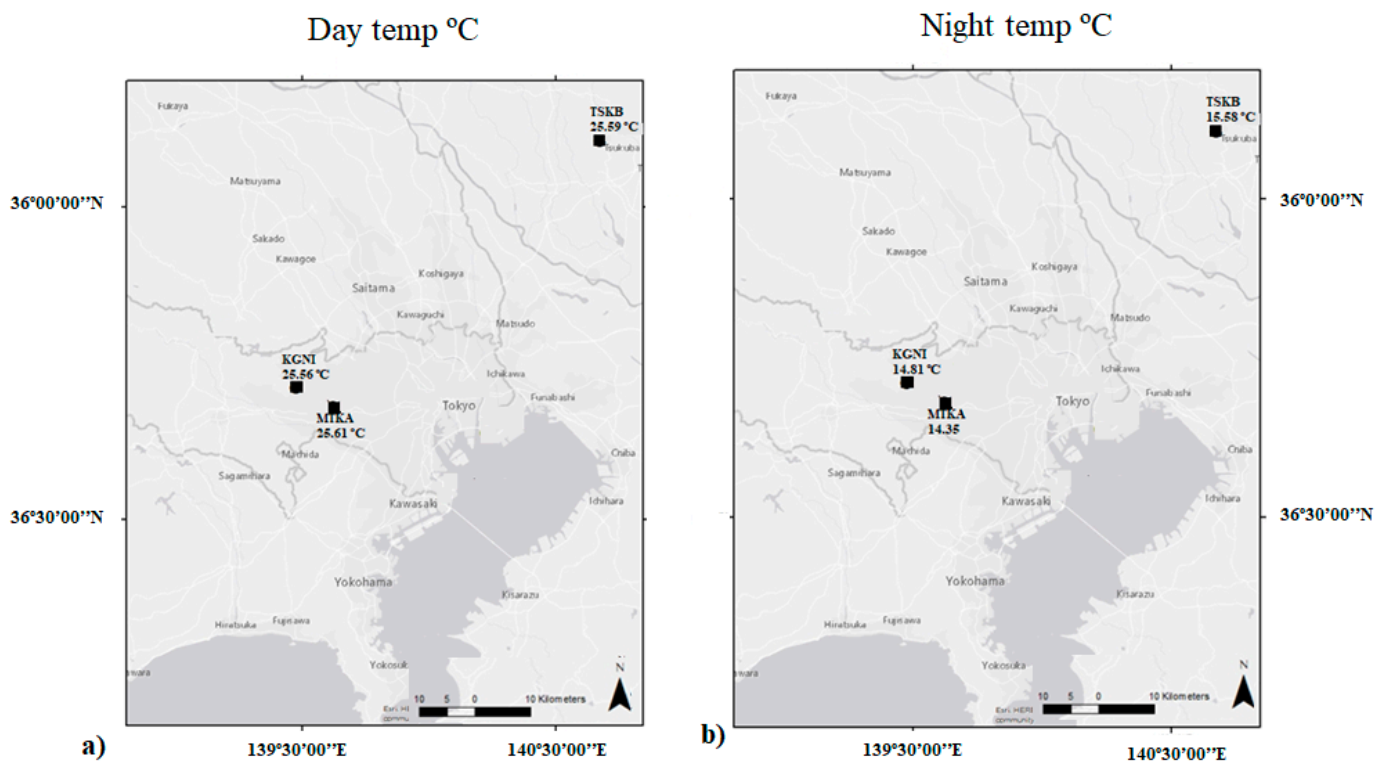


Figure 4. (a) Average temperatures in the summer (June to September) during the day (08:00 to 20:00 (UTC+9) local time LT). (b) Average temperatures in the summer during the night (20:00–08:00 LT).

The diurnal cycle of the AUHI, as shown in Figure 5, is similar to the diurnal cycle of the AUHI in Hong Kong.

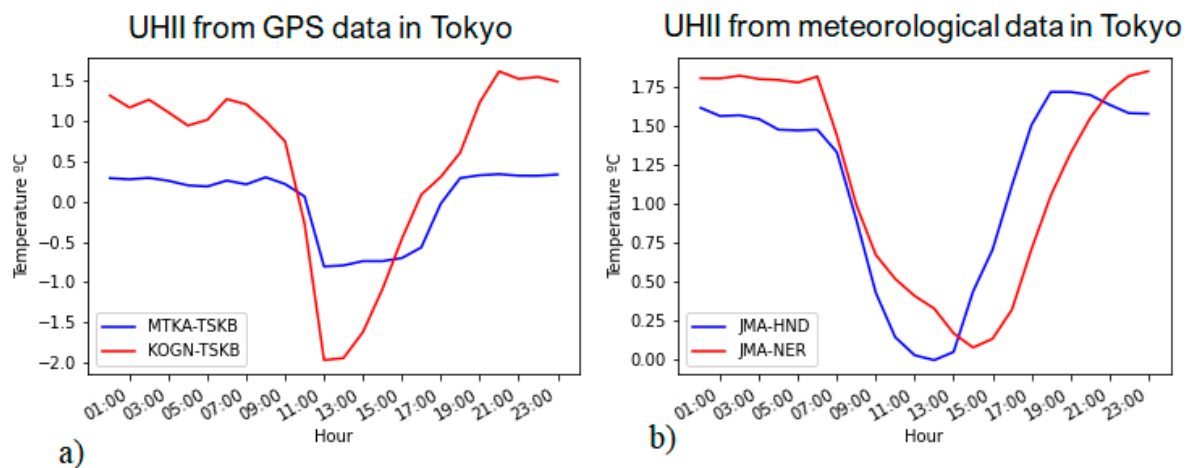


Figure 5. AUHI intensity in Tokyo (a) estimated with GPS data and (b) measured with meteorological data. Local time in Tokyo is UTC+9.

As shown in Figure 5, the intensity of the AUHI in Tokyo remains almost constant during the first 7 h of the day, then it decreases, reaching its minimum value at 13:00 LT. The maximum value is reached at 20:00 and then the intensity remains almost unchanged through the night. The negative intensity found with GPS data is due to an underestimation of the water vapor partial pressure.

5.3. Validation of the Proposed Method

The validation of the proposed method presented in this paper was achieved by comparing the AUHI obtained from GPS data and the AUHI measured with meteorological data during the summer, as shown in Figures 3 and 5. In HK, the UHI was defined between station hkoh-hksl and station hkst-hksl because those stations clearly define an urban-like and a rural-like area, respectively. The mean absolute error (MEA) indicates the accuracy of the presented algorithm. The MEA for stations in Hong Kong and Japan are shown in Table 4.

Table 4. Mean absolute error.

	Stations	MEA [°C]
Hong Kong	hkoh-hksl	0.85
	hkst-hksl	0.74
Tokyo	mtka-tskb	0.22
	kogn-tskb	0.25

In order to validate the algorithm with different weather conditions, data were divided by months. All daily averages of the same month from GPS data were compared to the daily averages of the same month from meteorological data. The monthly mean absolute error (confidence interval CI 95%) obtained for data from Hong Kong and Tokyo are shown in Figure 6a,b, respectively.

The lowest mean absolute error (MAE) can be found in January in Hong Kong (HKOH as urban station) and in July in Tokyo, while the highest MAE can be found in September in Hong Kong (HKOH as urban station) and December in Tokyo. Water vapor pressure seems to be estimated better during the dry season in Tokyo and the wet season in Hong Kong. Therefore, the MEA is lower during those months, as shown in Figure 6. Further research to understand the effect of each meteorological variables in the GPS signal would be required to improve this algorithm.

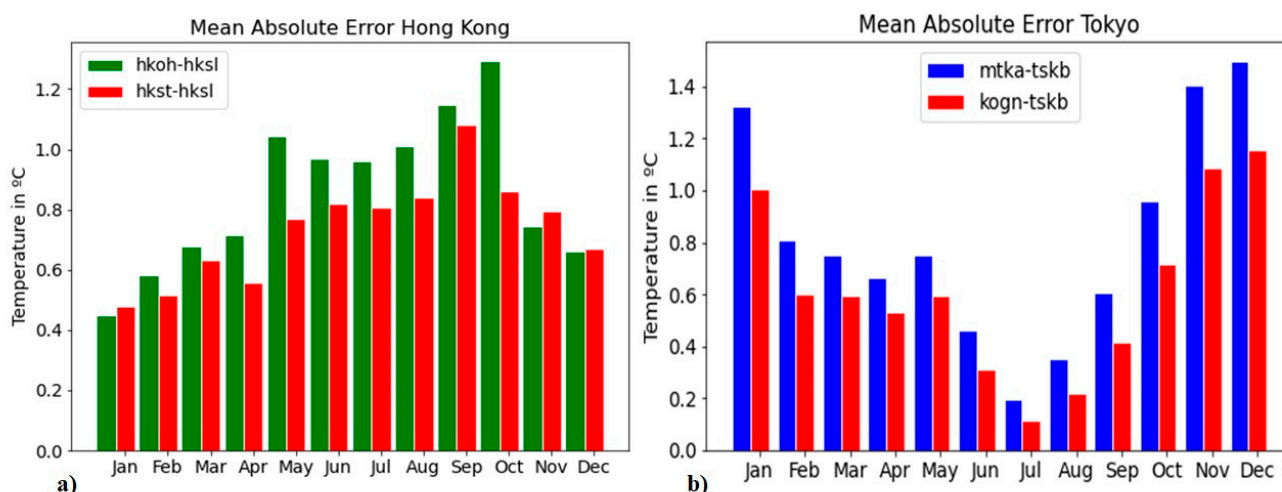


Figure 6. (a) Mean absolute error for data in Hong Kong. (b) Mean absolute error for data in Tokyo.

6. Discussion

The proposed approach had an overall average MAE of 0.24 °C in Tokyo and 0.79 °C in Hong Kong. This is an improvement over the previously obtained 1.71 °C MAE with average monthly data [13]. Furthermore, the use of hourly data enabled us to better capture the diurnal cycle and the differences in time, which were not detected when using monthly data. However, the main challenge of this approach is the computation of water vapor pressure, since water vapor changes rapidly and is hard to model. The other environmental variables needed in this algorithm can be easily obtained from weather stations or weather models.

The advantages of this approach are that ZTD can be estimated in real time [41] and that GPS data are available under all weather conditions. Furthermore, recently data collected with smartphones GPS receivers have been processed using PPP [42,43]. Thus, existing GPS infrastructure can be exploited to monitor the UHI with high precision. The potential use of existing GPS infrastructure and embedded GPS receivers would allow monitoring of the spatial distribution of the AUHI using big sensor networks built without additional costs. The advantage of using hourly data instead of daily averages to estimate UHI intensity is that the diurnal cycle of the AUHI can be obtained. Furthermore, the algorithm performs better than the one used in a previous study [13] because some the water vapor pressure changes are taken into account in this approach.

The diurnal cycle of the AUHI estimated with GPS data and measured with meteorological data in Hong Kong and Tokyo followed similar patterns. During the hours of 08:00–20:00 local time, the UHI intensity reached its minimum values, while at night the maximum values were reached in both cities. Similar patterns to the ones reported here were found in previous research [20]. The difference in warming rates during daytime and night-time can be explained by the formation of a strong stable layer during night-time and the development of a mixed layer during the daytime [44].

The spatial distribution of temperatures estimated from GPS data in Hong Kong clearly showed the UHI during the night when the temperature differences across stations in the territory were greater than during the day. In this case, the spatial distribution of the UHI in Tokyo requires inputs from more stations to be computed clearly. This challenge can be overcome with data from other GPS receivers or using machine learning and historic data [26].

The potential of this technique to be used to monitor extreme heat events around a city is high. With this technique, we could provide real-time or near-real-time air temperature data, which could be exploited by city planners or by citizens to avoid extreme heat exposure. The advantage is that there is no need to deploy new sensors because devices such as smartphones with embedded GPS receivers could be used to estimate temperature.

7. Conclusions

The test cases show that it is possible to monitor the diurnal cycle of the air urban heat island intensity in the urban canopy layer using the relation of the GNSS-derived ZTD and the refractivity of the troposphere defined in terms of temperature, air pressure, and water vapor partial pressure. The validation of the algorithm, which was achieved using data from Hong Kong and Tokyo, showed that the overall performance of the algorithm makes it attractive for use in studying the spatial distribution of urban heat islands. Furthermore, this approach could be used to provide near real-time AUHI data with existing infrastructure to monitor extreme heat events in urban areas.

Author Contributions: Conceptualization, J.M.-A. and L.L.; methodology, L.L.; software, J.M.-A.; validation, Y.-T.T., L.L., and J.M.-A.; formal analysis, Y.-T.T.; investigation, L.L.; resources, T.M.; data curation, T.M.; writing—original draft preparation, J.M.-A.; writing—review and editing, L.L., Y.-T.T., and T.M.; visualization, J.M.-A.; supervision, T.M.; project administration, L.L.; funding acquisition, L.L. and J.M.-A. All authors have read and agreed to the published version of the manuscript.

Funding: The APC was funded by the International Doctoral Training Centre, Ningbo Education Bureau, Ningbo Science and Technology Bureau and the University of Nottingham, and the UK Engineering and Physical Sciences Research Council [grant number [EP/L015463/1].

Institutional Review Board Statement: Not applicable.

Informed Consent Statement: Not applicable.

Data Availability Statement: The GNSS and meteorological data from Hong Kong that support the findings of this study are openly available in the site of Hong Kong Geodetic Survey System at [<ftp://ftp.geodetic.gov.hk/>] (accessed on 3 November 2021)]. The GNSS data from Tokyo are openly available in the site of the International GNSS service at [<https://cddis.nasa.gov/archive/gnss/data/daily>] (accessed on 3 November 2021)]. Meteorological data from Tokyo are openly available in the site of the Japan Meteorological Agency at [<https://www.data.jma.go.jp/gmd/risk/obsdl/>] (accessed on 3 November 2021)] in Japanese. Radiosonde data are openly available in the site of the Integrated Global Radiosonde Archive at [<https://www1.ncdc.noaa.gov/pub/data/igra/>] (accessed on 3 November 2021)].

Acknowledgments: The first author acknowledges the National Autonomous University of Mexico (UNAM)'s postdoctoral fellowship. Furthermore, the authors acknowledge the financial support from the International Doctoral Training Centre, Ningbo Education Bureau, Ningbo Science and Technology Bureau and the University of Nottingham.

Conflicts of Interest: The authors declare no conflict of interest.

Appendix A

Images used for LCZ classification of GPS and meteorological stations in Tokyo, Japan, and Hong Kong, China.

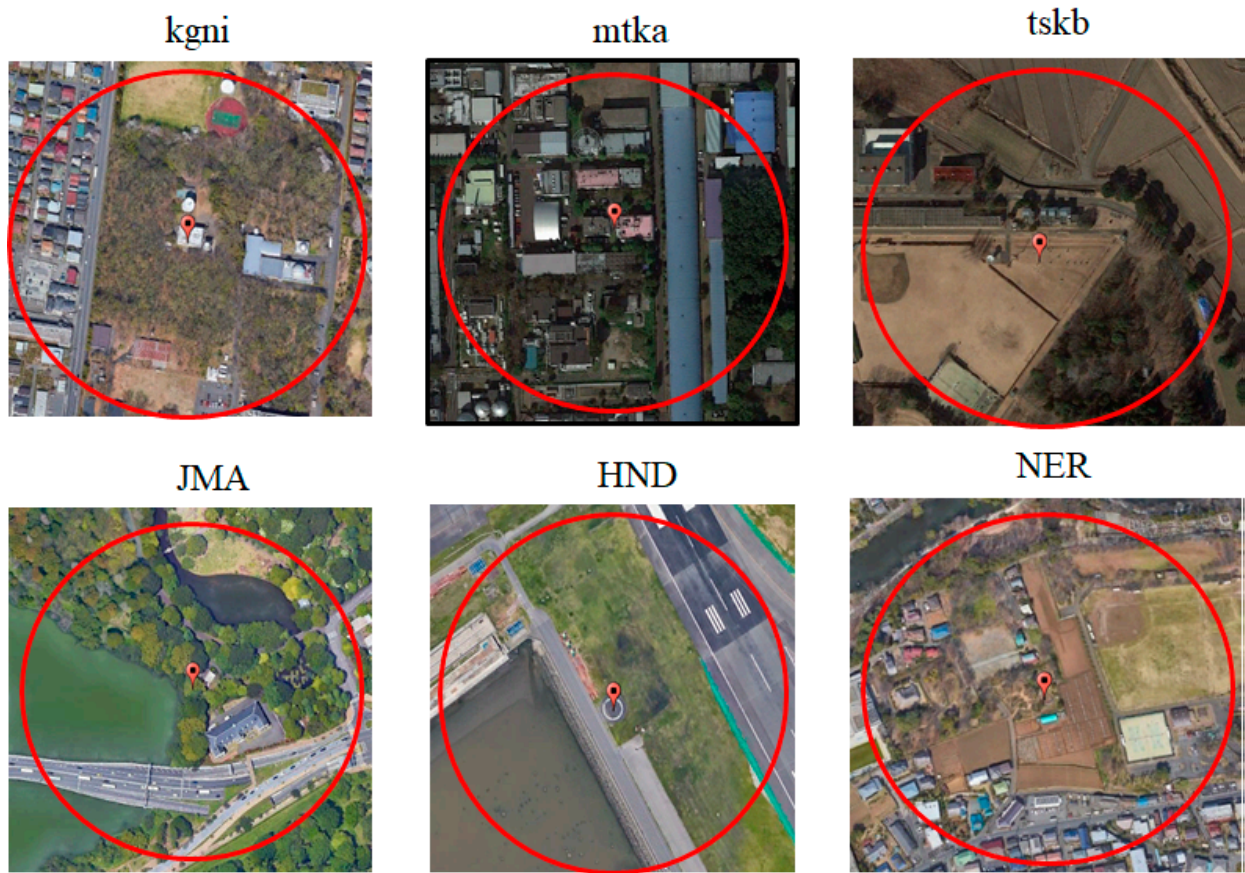


Figure A1. Surroundings of all GNSS and meteorological stations in Tokyo, Japan.

Stations in Hong Kong

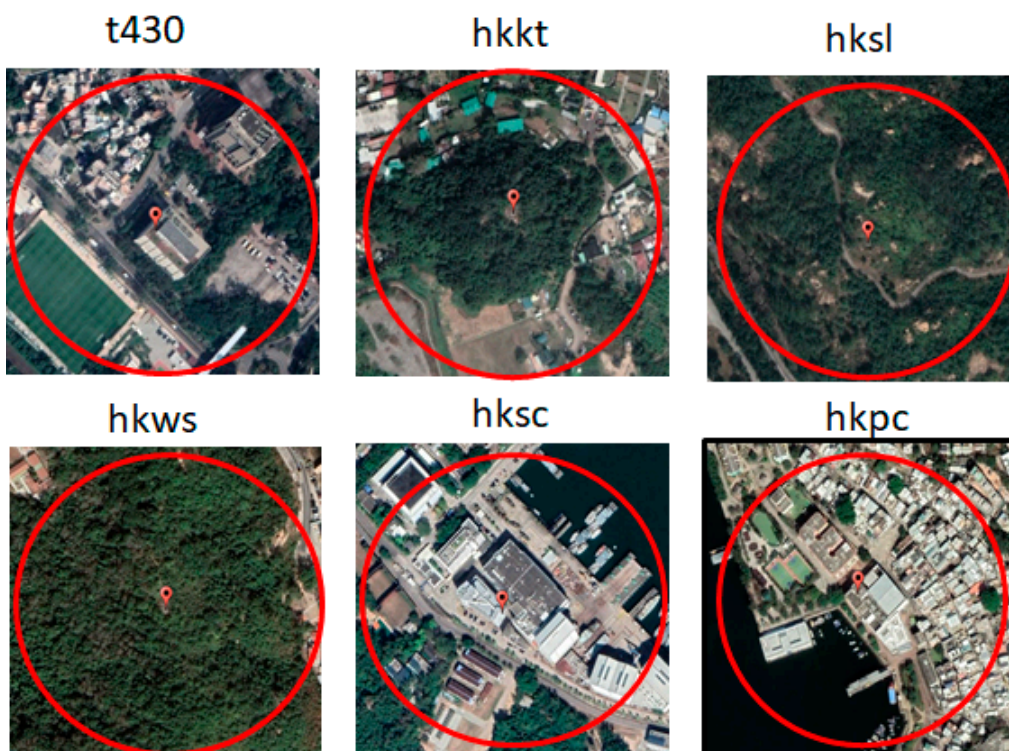


Figure A2. Surroundings of all GNSS and meteorological stations in Hong Kong, China.

References

1. Roth, M. Urban Heat Island. In *Handbook of Environmental Fluid Dynamics*; Fernando, H.J.S., Ed.; Taylor & Francis Group: Abingdon, UK, 2013; Volume II, pp. 143–159.
2. United Nations. World Population Prospects. 2018. Available online: <https://population.un.org/wpp/> (accessed on 16 November 2021).
3. Huang, K.; Li, X.; Liu, X.; Seto, K.C. Projecting global urban land expansion and heat island intensification through 2050. *Environ. Res. Lett.* **2019**, *14*, 114037. [[CrossRef](#)]
4. Tuholske, C.; Caylor, K.; Funk, C.; Verdin, A.; Sweeney, S.; Grace, K.; Peterson, P.; Evans, T. Global urban population exposure to extreme heat. *Proc. Natl. Acad. Sci. USA* **2021**, *118*, e2024792118. [[CrossRef](#)] [[PubMed](#)]
5. Khosla, R.; Jani, A.; Perera, R. Editorial: Health risks of extreme heat. *BMJ* **2021**, *375*, n2438. [[CrossRef](#)]
6. Zhang, Y.; Li, D.; Liu, L.; Liang, Z.; Shen, J.; Wei, F.; Li, S. Spatiotemporal Characteristics of the Surface Urban Heat Island and its Driving Factors Based on Local Climate Zones and Population in Beijing, China. *Atmosphere* **2021**, *12*, 1271. [[CrossRef](#)]
7. Gawuc, L.; Jefimow, M.; Szymankiewicz, K.; Kuchcik, M.; Sattari, A.; Struzewska, J. Statistical Modeling of Urban Heat Island intensity in Warsaw, Poland Using Simultaneous Air and Surface Temperature Observations. *IEEE J. Sel. Top. Appl.* **2020**, *13*, 2716–2728. [[CrossRef](#)]
8. Yu, K.; Rizos, C.; Burrage, D.; Dempster, A.G.; Zhang, K.; Markgraf, M. An overview of GNSS remote sensing *EURASIP J. Adv. Signal Process.* **2014**, *2014*, 134. [[CrossRef](#)]
9. Yu, C.; Penna, N.T.; Li, Z. Generation of real-time mode high-resolution water vapor fields from GPS observations. *J. Geophys. Res. Atmos.* **2017**, *122*, 2008–2025. [[CrossRef](#)]
10. Campos-Arias, P.; Esquivel-Hernández, G.; Valverde-Calderón, J.F.; Rodríguez-Rosales, S.; Moya-Zamora, J.; Sánchez-Murillo, R.; Boll, J. GPS Precipitable Water Vapor Estimations over Costa Rica: A comparison against atmospheric sounding and Moderate Resolution Imaging Spectrometer (MODIS). *Climate* **2019**, *7*, 63. [[CrossRef](#)]
11. Monico, J.F.G.; Marques, H.A.; Tsuchiya, I.; Oyama, R.T.; Queiroz, W.R.S.; Wentz, J.P. Real Time PPP Applied to Airplane Flight Tests. *Bol. Cienc. Geod.* **2019**, *25*, e2019009. [[CrossRef](#)]
12. Shinghal, G.; Bisnath, S. Conditioning and PPP processing of smartphone GNSS measurements in realistic environments. *Satell. Navig.* **2021**, *2*, 10. [[CrossRef](#)]
13. Mendez-Astudillo, J.; Lau, L.; Tang, Y.T.; Moore, T. A new Global Navigation Satellite System (GNSS) based method for urban heat island intensity monitoring. *Int. J. Appl. Earth Obs. Geoinf.* **2021**, *94*, 102222. [[CrossRef](#)]
14. Statista. Number of Smartphone Users from 2016 to 2021. Available online: <https://www.statista.com/statistics/330695/number-of-smartphone-users-worldwide> (accessed on 8 September 2021).
15. Giridharan, R.; Ganesan, S.; Lau, S.S.Y. Daytime urban heat island effect in high-rise and high-density residential developments in Hong Kong. *Energy Build.* **2004**, *36*, 525–534. [[CrossRef](#)]
16. Giridharan, R.; Lau, S.S.Y.; Ganesan, S. Nocturnal heat island effect in urban residential developments of Hong Kong. *Energy Build.* **2005**, *37*, 964–971. [[CrossRef](#)]
17. Giridharan, R.; Lau, S.S.Y.; Ganesan, S.; Givoni, B. Urban design factors influencing heat island intensity in high-rise high-density environments of Hong Kong. *Build Environ.* **2007**, *42*, 3669–3684. [[CrossRef](#)]
18. Fung, W.Y.; Lam, K.S.; Nichol, J.E.; Wong, M.S. Derivation of nighttime urban air temperature using a satellite thermal image. *J. Appl. Meteorol. Clim.* **2009**, *48*, 863–872. [[CrossRef](#)]
19. Nichol, J.E.; Fung, W.Y.; Lam, K.S.; Wong, M.S. Urban heat island diagnosis using ASTER satellite images and ‘in situ’ air temperature. *Atmos. Res.* **2009**, *94*, 276–284. [[CrossRef](#)]
20. Siu, L.W.; Hart, M.A. Quantifying urban heat island intensity in Hong Kong SAR, China. *Environ. Monit. Assess.* **2013**, *185*, 4383–4398. [[CrossRef](#)]
21. Chen, X.; Jeong, S.-J. Shifting the urban heat island clock in a megacity: A case study of Hong Kong. *Environ. Res. Lett.* **2018**, *13*, 014014. [[CrossRef](#)]
22. Yoshikado, H.; Tsuchida, M. High levels of winter air pollution under the influence of the Urban Heat Island along the shore of Tokyo Bay. *J. Appl. Meteorol.* **1996**, *35*, 1804–1813. [[CrossRef](#)]
23. Hirano, Y.; Fujita, T. Evaluation of the impact of the urban heat island on residential and commercial energy consumption in Tokyo. *Energy* **2012**, *37*, 371–383. [[CrossRef](#)]
24. Matsumoto, J.; Fujibe, F.; Takahashi, H. Urban climate in the Tokyo metropolitan area in Japan. *J. Environ. Sci.* **2017**, *59*, 54–62. [[CrossRef](#)] [[PubMed](#)]
25. Varquez, A.C.G.; Kanda, M. Global urban climatology: A meta-analysis of air temperature trends (1960–2009). *NPJ Clim. Atmos. Sci.* **2018**, *1*, 32. [[CrossRef](#)]
26. Mendez-Astudillo, J.; Mendez-Astudillo, M. A Machine Learning Approach to Monitoring the UHI from GNSS Data. *IEEE Trans. Geosci. Remote* **2022**, *60*, 1–11. [[CrossRef](#)]
27. Stewart, I.D.; Oke, T.R. Local climate zones for urban temperature studies. *Bull. Am. Meteorol. Soc.* **2012**, *93*, 1879–1900. [[CrossRef](#)]
28. Japan Meteorological Agency. Surface Observation. Available online: <https://www.jma.go.jp/jma/en/Activities/surf/surf.html> (accessed on 2 October 2021).
29. Statistics Bureau of Japan. Population and Households of Japan. Available online: http://www.stat.go.jp/english/data/kokusei/2015/final_en/final_en.html#Summary (accessed on 31 August 2021).

30. HKGSS. Hong Kong Satellite Positioning Reference Station Network (SatRef). Available online: <https://www.geodetic.gov.hk/en/satref/satref.htm> (accessed on 10 December 2020).
31. International GNSS Service. CDDIS Daily 30-Second Data. Available online: https://cddis.nasa.gov/Data_and_Derived_Products/GNSS/daily_30second_data.html (accessed on 10 December 2020).
32. IGRA. Integrated Global Radiosonde Archive. Available online: <https://www.ncdc.noaa.gov/data-access/weather-balloon/integrated-global-radiosonde-archive> (accessed on 2 October 2021).
33. Stewart, I.D.; Oke, T.R.; Krayenhoff, E.S. Evaluation of the ‘local climate zone’ scheme using temperature observations and model simulations. *Int. J. Climatol.* **2014**, *34*, 1062–1080. [[CrossRef](#)]
34. Heroux, P.; Kouba, J. GPS precise point positioning using IGS orbit products. *Phys. Chem. Earth Part A* **2001**, *26*, 573–578. [[CrossRef](#)]
35. Gao, Y. GNSS Solutions: Precise Point Positioning and its Challenges. *Inside GNSS* **2006**, November–December 2016, 16–18. Available online: <https://www.insidegnss.com/auto/NovDec06GNSSolutions.pdf> (accessed on 25 January 2022).
36. Mendez-Astudillo, J.; Lau, L.; Tang, Y.T.; Moore, T. Analysing the Zenith Tropospheric Delay Estimates in On-line Precise Point Positioning (PPP) Services and PPP Software Packages. *Sensors* **2018**, *18*, 580. [[CrossRef](#)]
37. Stull, R. Chapter 4. Water Vapor. In *Practical Meteorology: An Algebra-Based Survey of Atmospheric Science*; The University of British Columbia: Vancouver, BC, Canada, 2017; Volume 1.02b.
38. Hofmann-Wellenhof, B.; Lichtenegger, H.; Waskle, E. *GNSS-Global Navigation Satellite Systems GPS, GLONASS, Galileo and More*; Springer: Vienna, Austria, 2008.
39. Lasota, E.; Rohm, W.; Guerova, G.; Liu, C.-Y. A comparison between ray-traced GFS/WRF/ERA and GNSS Slant Path Delays in tropical cyclone Meranti. *IEEE Trans. Geosci. Remote* **2020**, *58*, 421–435. [[CrossRef](#)]
40. Mendez-Astudillo, J. Investigation into UHI Monitoring with GNSS Sensor Network. Ph.D. Thesis, University of Nottingham Ningbo China, Ningbo, China, 2020.
41. Alkan, R.M.; Erol, S.; Ilci, V.; Murat Ozulu, I. Comparative analysis of real-time kinematic and PPP techniques in dynamic environment. *Measurement* **2020**, *163*, 107995. [[CrossRef](#)]
42. Lachapelle, G.; Gratton, P. GNSS Precise Point Positioning with Android Smartphones and Comparison with High Performance Receivers. In Proceedings of the 2019 IEEE International Conference on Signal, Information and Data Processing (ICSIDP), Chongqing, China, 11–13 December 2019; pp. 1–9.
43. Wang, L.; Li, Z.; Wang, N.; Wang, Z. Real-Time GNSS precise point positioning for low-cost smart devices. *GPS Solut.* **2021**, *25*, 69. [[CrossRef](#)]
44. Sugimoto, S.; Sato, T.; Sasaki, T. Seasonal and diurnal variability in historical warming due to the urbanization of Hokkaido, Japan. *J. Geophys. Res.-Atmos.* **2015**, *120*, 5437–5445. [[CrossRef](#)]